

# Quantifying Electrochemical Degradation in Single-Crystalline $\text{LiNi}_{0.8}\text{Mn}_{0.1}\text{Co}_{0.1}\text{O}_2$ -Graphite Pouch Cells through *Operando* X-Ray and Postmortem Investigations


Ashok S. Menon<sup>1,2,\*</sup>, Nickil Shah,<sup>1</sup> James A. Gott,<sup>1</sup> Eleni Fiamégkou,<sup>1,2</sup> Matthew J. W. Ogley<sup>1,2</sup>, Galo J. Páez Fajardo<sup>1,2</sup>, Naoum Vaenas,<sup>1</sup> Ieuan Ellis<sup>1</sup>, N. Ravichandran,<sup>1</sup> P. Cloetens,<sup>3</sup> D. Karpov<sup>3</sup>, J.M. Warnett,<sup>1</sup> Paul Malliband,<sup>1</sup> David Walker,<sup>4</sup> Geoff West,<sup>1</sup> Melanie Loveridge<sup>1,2</sup>, and Louis F.J. Piper<sup>1,2,†</sup>

<sup>1</sup>Warwick Manufacturing Group, University of Warwick, Coventry CV4 7AL, UK

<sup>2</sup>The Faraday Institution, Quad One, Harwell Campus, Didcot OX11 0RA, UK

<sup>3</sup>European Synchrotron Radiation Facility, Grenoble 38000, France

<sup>4</sup>Department of Physics, University of Warwick, Coventry CV4 7AL, UK

 (Received 23 June 2023; revised 5 December 2023; accepted 18 December 2023; published 23 January 2024)

Layered nickel-rich lithium transition-metal oxides ( $\text{LiNi}_x\text{Mn}_y\text{Co}_{1-x-y}\text{O}_2$ ; where  $x \geq 0.8$ ), with single-crystalline morphology, are promising future high-energy-density Li-ion battery cathodes due to their ability to mitigate particle-cracking-induced degradation. This is due to the absence of grain boundaries in these materials, which prevents the build-up of bulk crystallographic strain during electrochemical cycling. Compared to their polycrystalline counterparts, there is a need to study single-crystalline Ni-rich cathodes using *operando* x-ray methods in uncompromised machine-manufactured industrylike full cells to understand their bulk degradation mechanisms as a function of different electrochemical cycling protocols. This can help us identify factors to improve their long-term performance. Here, through in-house *operando* x-ray studies of pilot-line-built  $\text{LiNi}_{0.8}\text{Mn}_{0.1}\text{Co}_{0.1}\text{O}_2$ -graphite A7 pouch cells, it is shown that their electrochemical-capacity fade under harsh conditions (2.5–4.4 V and 40 °C for 100 cycles at a C/3 rate) primarily stems from the high-voltage reconstruction of the cathode surface from a layered to a cubic (rock-salt) phase that impedes the  $\text{Li}^+$  kinetics and increases cell impedance. Postmortem electron and x-ray microscopy show that these cathodes can withstand severe anisotropic structural changes and show no cracking when cycled under such conditions. Comparing these results to those from commercial Li-ion cells with surface-modified single-crystalline Ni-rich cathodes, it is identified that cathode surface passivation can mitigate this type of degradation and prolong cycle life. In addition to furthering our understanding of degradation in single-crystalline Ni-rich cathodes, this work also accentuates the need for practically relevant and reproducible fundamental investigations of Li-ion cells and presents a methodology for achieving this.

DOI: [10.1103/PRXEnergy.3.013004](https://doi.org/10.1103/PRXEnergy.3.013004)

## I. INTRODUCTION

Ni-rich NMC layered oxides ( $\text{LiNi}_x\text{Mn}_y\text{Co}_{1-x-y}\text{O}_2$ ; where  $x \geq 0.8$ ) are commercially viable cathode materials for future high-energy-density Li-ion batteries, provided that their performance can be stabilized against the various degradation pathways known to impact them [1,2].

\*ashok.menon@warwick.ac.uk

†Louis.Piper@warwick.ac.uk

Published by the American Physical Society under the terms of the [Creative Commons Attribution 4.0 International](https://creativecommons.org/licenses/by/4.0/) license. Further distribution of this work must maintain attribution to the author(s) and the published article's title, journal citation, and DOI.

Crystallographic strain-induced particle cracking during high-voltage electrochemical cycling is one such degradation mode that can trigger both interfacial and bulk degradation. During delithiation, Ni-rich cathode particles expand and contract along the crystallographic layer-stacking and basal directions to different degrees, i.e., in an anisotropic manner [3–5]. Although reversible during lithiation, repeated occurrences of this phenomenon, termed anisotropic “lattice” collapse, create crystallographic strain within the particle bulk that can lead to (micro)cracking and eventual intergranular fracture. This is true for polycrystalline cathodes composed of primary particle aggregates due to the presence of particle-grain boundaries that serve as hot beds for stress build-up and nucleation of cracks. This increases the exposure of

particles to deleterious electrolyte-electrode reactions at their interface, among other factors that result in capacity fade and voltage hysteresis [2,3]. Overcoming this problem through material engineering is key to stabilizing the long-term electrochemical performance of the cathode. Grain-boundary-free single-crystalline cathodes, with individual particles (typically 3–5  $\mu\text{m}$  in size) that do not cluster or agglomerate, offer a potential solution. They resist cracking under most conditions [6–14] and only show traces of shearing-induced intragranular cracks at voltages as high as 4.4 V (versus graphite) [9,12,15]. Additionally, they also exhibit comparatively smaller gas evolution at high voltages and temperatures than polycrystalline cathodes [7]. Therefore, Ni-rich cathodes with single-crystalline morphology can potentially offer the best of both worlds: increased energy density at high voltages with suppressed particle-cracking-induced degradation.

Difficulties in the large-scale synthesis of single-crystalline Ni-rich NMC cathodes have limited studies into how long-term electrochemical cycling under industry-relevant full-cell conditions affects their structural, interfacial, and morphological properties [16,17]. In contrast, many such studies have been performed for full cells with polycrystalline Ni-rich NMC cathodes [18–28]. Although complex [29], electrochemical capacity loss in such cells can be broadly categorized as irreversible and reversible based on their origins. Irreversible capacity loss occurs via the consumption of electrochemically active Li ions ( $\text{Li}^+$ ) during the solid-electrolyte interphase (SEI) layer build-up on the anode. Although this primarily occurs during the initial formation cycles, the SEI layer continues to grow with cycling, decreasing the active  $\text{Li}^+$  concentration in the cell (loss of Li inventory). This results in the misalignment of electrode capacities relative to the start (electrode slippage), thereby shifting their operational voltage window and causing the cathode to cycle at higher states of charge (SOCs) [30,31]. At such SOCs and high voltages, Ni-rich cathodes lose oxygen from the surface [32–34]. Consequently, the cathode surface “reconstructs” to compensate for the O deficiency by transforming from the layered to cubic (rock-salt and/or spinel) phases, creating a surface layer with reduced transition-metal (TM) species [20,25,30,35,36]. These species can also lead to TM dissolution from the cathode to the anode, which can adversely affect the SEI layer and contribute to capacity fade [26,27,36–38]. Additionally, the evolved O can also chemically oxidize the electrolyte (in addition to high-voltage electrolyte decomposition, if any) to form resistive cathode-electrolyte interphase (CEI) layers. Although deconvoluting the influence of cycling parameters on the structure, composition, and thickness of these cathode surface layers is challenging [39], it is clear that they increase the cell impedance by worsening the  $\text{Li}^+$  transport kinetics. This is exacerbated in polycrystalline cathodes, where particle cracking further increases the exposed area and

promotes impedance growth [3–5]. In Ni-rich NMC cathodes cycled at high voltages, the rock-salt surface layer has been found to be the dominant factor contributing to the cell-impedance rise and therefore primarily responsible for the reversible capacity loss that occurs in these systems with long-term cycling [14,24,39]. This is dependent on the cycling rate (i.e., applied current) and some of the “lost” capacity may be recovered through slower cycling. Long-term *operando* x-ray studies of Ni-rich cathode full cells have also shown that the formation of surface rock-salt phases can lead to cathode bulk being segregated into “active” and “fatigued” phases, which have reduced  $\text{Li}^+$  mobility [18–20]. Interestingly, the same factors also apply to single-crystalline cathodes to a certain extent. Upon high-voltage cycling, single-crystalline Ni-rich cathodes can also reconstruct their surface into a rock-salt layer that impedes  $\text{Li}^+$  diffusion, increasing cell impedance [14]. The resulting sluggish  $\text{Li}^+$  kinetics in such micron-sized cathode particles lead to a surface-to-bulk  $\text{Li}^+$  concentration gradient that can generate internal stresses that might adversely affect high(er)-rate and long-term cycling [15]. Evaluating these phenomena in single-crystalline Ni-rich NMC cathodes under industry-relevant full-cell conditions and how they impact their material properties will be key to further understanding their degradation behavior.

Degradation pathways in Li-ion battery cells primarily depend on electrode chemistry and cycling conditions. They are also subject to the cell manufacturing-process parameters, including—but not limited to—electrode formulation and fabrication (e.g., electrode coat weight, thickness, and porosity), and the cell formats [29]. As highlighted in recent publications, it is critical that when investigating industrially relevant issues such as the cell performance, degradation, and applicability of novel material-engineering strategies, they must be evaluated in conditions as close to their real-world operation as is reasonably possible [40–42]. Only then can the results obtained from such experiments be translated into meaningful and practical performance gains. However, accurate real-world representative investigations of Li-ion battery degradation are not a trivial endeavor. For example, although *operando* x-ray diffraction (XRD) and absorption spectroscopy are ideal probes of real-time electrode bulk degradation, they are difficult to perform in a manner that gives optimal electrochemical performance and x-ray data quality simultaneously [43,44]. Consequently, *operando* experiments are usually, if not always, carried out using modified electrochemical cells to improve the signal-to-noise quality of the data. The degree of modification depends on the cell chemistry and the characterization technique, both of which can necessitate technique-dependent bespoke electrochemical cells for *operando* studies [43]. However, such cells are substantially dissimilar to their conventional (academic and industrial) counterparts and hence have limited cyclability under

standard electrochemical testing conditions. While such cells are useful for early-stage fundamental investigations, they are not suitable for practical evaluation of the long-term cycling and degradation of technologically mature Li-ion battery chemistries. In other words, *operando* investigations aimed at meaningfully studying the degradation of electrochemical cells must be performed using unmodified cells operated under real-world conditions.

As a step toward further understanding of degradation mechanisms in single-crystalline Ni-rich cathode full cells, their long-term bulk-structure evolution and particle-cracking behavior over 100 cycles are investigated in this work. This is accomplished through *operando* x-ray (diffraction and Ni K-edge absorption spectroscopy) and postmortem (electron and x-ray) microscopy studies of single-crystalline-LiNi<sub>0.8</sub>Mn<sub>0.1</sub>Co<sub>0.1</sub>O<sub>2</sub>-graphite A7 balanced full pouch cells of industry-relevant specifications. These cells, built at WMG's Battery Scale-up pilot line (TRL-5), are used for the in-house *operando* experiments without any modifications to aid x-ray transmission, thereby providing uncompromised electrochemical performance. Note that the same pilot-line cell was used for both *operando* diffraction and spectroscopy experiments, which is usually difficult considering their experimental requirements [20]. A comparatively harsh cycling condition—2.5–4.4 V at 40 °C with a C/3 cycling rate—was deliberately used to accelerate degradation. As mentioned before, the upper cutoff voltage is beyond the oxygen-evolution onset voltage for Ni-rich cathodes and

is particularly expected to expedite the cathode degradation [24,25,27,28,31–33,36,45]. The electrochemical performance of the pilot-line cell are also compared with commercial Li-ion battery full cells with surface-modified single-crystalline Ni-rich cathodes to highlight how cathode surface engineering can be leveraged to improve long-term cell performance.

## II. RESULTS AND DISCUSSION

### A. Comparison of pilot-line and commercial cells

The pilot-line and commercial cells have comparable positive (single-crystalline Ni-rich NMC) and negative (graphite) electrodes. However, they primarily differ in terms of their form factors, as shown in Fig. 1. The pilot-line pouch cells [Fig. 1(a)], fabricated in-house following optimized industry-relevant protocols, are made of single-sided electrodes. The commercial cells [Fig. 1(b)] are 402035-type cells obtained from LiFun Technology, with double-sided electrodes wound together in a flattened “jellyroll” configuration, similar to those used in other studies [36,46–48]. Cross-section scanning-electron-microscopy (SEM) images of the cathodes are shown in the right-hand panels of Figs. 1(a) and 1(b) (for wider images, see Fig. S1 in the Supplemental Material [73]). The cathode-coating thicknesses are comparable, with the constituent particles in each case being single-crystalline micron-sized entities, albeit isolated agglomerates. Although both cathodes are predominantly Ni-rich ( $\geq 80$  at.% of the overall TM

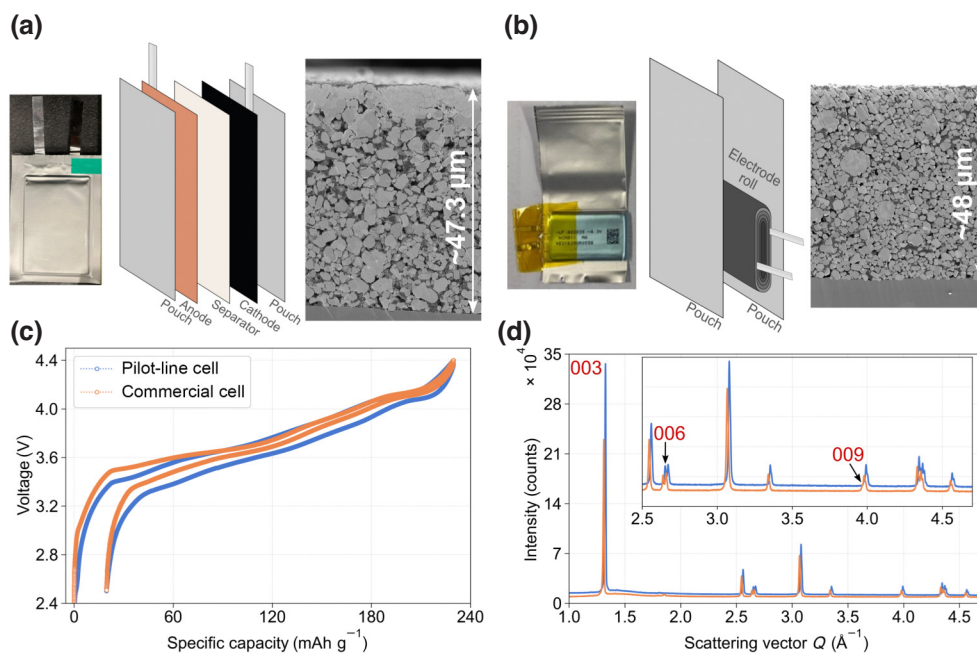


FIG. 1. A photograph (left) and an illustration (center) of the (a) pilot-line and (b) commercial pouch cells, with the corresponding cross-section SEM image of their cathodes. (c) The voltage-capacity plot of the first formation cycle of each cell. (d) The XRD pattern of the pilot-line and commercial cell cathodes, with higher- $Q$  regions magnified in the inset. The  $00l$  planes are highlighted. Parts (c) and (d) are color coordinated.

content), the commercial-cell cathodes have a slightly higher Ni content and, crucially, a proprietary Al-based surface-layer coating [7]. As per our previous study on the same cathodes, the Al surface layer mitigates the cathode surface degradation by scavenging hydrofluoric acid species and reducing TM dissolution, thereby improving the cell cycle life [49], conforming to previous studies [12,50–52]. Therefore, comparing the two cells permits the scrutiny of how the surface-modified cathode improves the cycling performance of the commercial cell, from a structural and morphological perspective. The pilot-line and commercial cells were subjected to the same formation cycles (2.5–4.4 V at an approximately  $C/20$  rate at 40 °C; for the voltage-time profiles, see Fig. S2 in the Supplemental Material [73]) and as seen in Fig. 1(c), comparable capacities are obtained. XRD data collected on the pristine pilot-line and commercial cathodes are shown in Fig. 1(d). Both data sets can be indexed using an  $R\bar{3}m$  unit cell, barring the weak peaks corresponding to the conductive carbon additive and Al current collector (see Fig. S3 in the Supplemental Material [73]). The refined unit-cell parameters are comparable and are shown in Table S1 in the Supplemental Material [73]. The electrodes show preferred orientation along the crystallographic 00 $l$  direction, as evidenced by the increased intensity of those reflections [highlighted in Fig. 1(d)], similarly to a previous study [48]. Although structural refinements were not performed due to uncertainties in the stoichiometry and preferred orientation, the XRD data suggests that the cathodes have comparable bulk structural properties despite the surface

modification in the commercial cathode. Having confirmed that cathodes have comparable morphological, structural, and electrochemical properties, their longer-term electrochemical performance was compared.

The mean absolute and normalized discharge capacities of three pilot-line and commercial cells each, cycled 100 times between 2.5 and 4.4 V at 40 °C using a  $C/3$  rate (following formation), are shown in Figs. 2(a) and 2(b), respectively. Both kinds of cells show similar electrochemical performance, with a virtually linear capacity decay over the course of cycling. The commercial cells, due to their higher Ni content, initially exhibit approximately 10.5 mAh  $g^{-1}$  higher capacity than the pilot-line cell, which increases to >13 mAh  $g^{-1}$  after 100 cycles. The 40 °C cycling also contributes to higher discharge capacities than is normal due to the improved charge-transfer reaction kinetics [53]. As per Fig. 2(b), the pilot-line cell shows approximately 2% higher capacity fade after 100 cycles, which is expected to widen over further cycling. Nevertheless, despite the wide voltage window and elevated cycling temperature, no significant performance deterioration—apart from the gradual capacity loss—is seen. The charge and discharge voltage profiles during the first (gray) and 100th (colored) cycles from one pilot-line (triangles) and commercial (circles) cell each are shown in Fig. 2(c). The evolution of the voltage profiles is typical of cell-impedance growth (and kinetic polarization) and electrode slippage [24,31,54]. The same factors are present in both cells, albeit to different degrees. Expectedly, lower voltage hysteresis is seen in the commercial

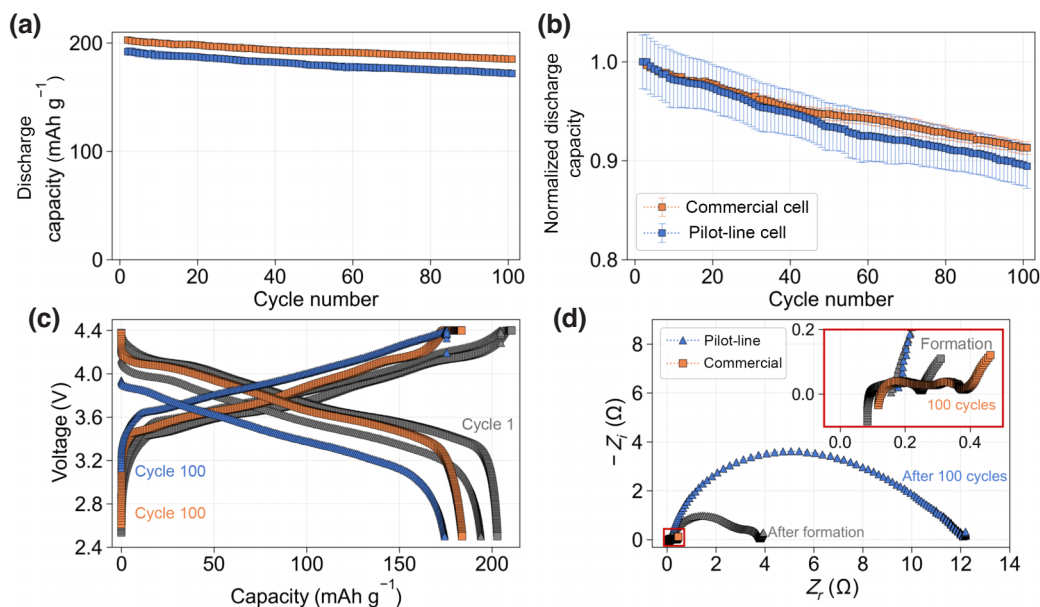


FIG. 2. The (a) absolute and (b) normalized discharge capacities of the pilot-line and commercial cells. (c) The charge- and discharge-voltage profiles during the first (gray) and 100th (colored) cycles for the pilot-line (triangles) and commercial (circles) cells. (d) The EIS data measured after formation and 100 cycles on the pilot-line and commercial cells, shown as Nyquist plots. Note that the top- and bottom-panel plots are color coordinated.



cell due to the surface-modified cathode [50,51]. The same trend is also observed in the cell-impedance growth as per the electrochemical impedance spectroscopy (EIS) data [Fig. 2(d)]. As is typical for NMC-graphite cells, three distinct features are visible in the EIS data: two (partial) semicircles at high- and midfrequencies (corresponding to the surface-layer and charge-transfer contributions, respectively), and a Warburg-type impedance tail (reflecting solid-state  $\text{Li}^+$  diffusion) at lower frequencies [55]. In the pilot-line cell data collected after formation, the high- and midfrequency semicircles overlap but are distinguishable. After 100 cycles, the overlap increases and a significant increase in the cell impedance is seen. At this stage, the impedance value at the intersection of the mid-frequency semicircle and the Warburg tail increases from  $3.78 \Omega$  to  $12.12 \Omega$ , with corresponding frequency values of 0.23 and 0.07 Hz, respectively. The impedance increase in NMC-graphite systems subjected to similar high-voltage cycling protocols has been previously primarily attributed to the formation of the resistive rock-salt surface layer on the cathode and not to electrolyte degradation and its byproducts (CEI) [24,34]. As expected, due to the protective Al-surface doping, markedly lower impedance (up to an order of magnitude), is seen in the commercial-cell EIS data [50,51]. For comparison, the corresponding impedance at the intersection of the midfrequency semicircle and the Warburg tail for the postformation, and 100 cycles are 0.25 and 0.39  $\Omega$ , respectively. Form-factor and architecture dissimilarities between the pilot-line and

commercial cells might also lead to differences observed in the EIS data to some degree [56]. Nonetheless, despite the unmodified NMC cathode, the pilot-line cells show satisfactory electrochemical performance during the first 100 cycles compared to that of commercial cells and so are ideal for real-world representative *operando* x-ray investigations.

### B. *Operando* studies using pilot-line cells

Figure 3(a) shows the setup of the pilot-line cells on the in-house x-ray instruments for the *operando* experiments. The electrochemical cycling data from the XRD and Ni K-edge x-ray absorption near edge structure (XANES) spectroscopy experiments are shown in Fig. 3(b). The XRD (cycles 1 and 101) and XANES (cycles 2 and 102) experiments were always performed back to back, using the same pilot-line cell. However, the postformation (cycles 1 and 2) and 100-cycles (cycles 101 and 102) experiments were carried out using different cells, to ensure that the 100-cycle cell did not suffer from ageing-induced performance fade due to down time between the *operando* and regular cycling steps. The *operando* experiments comprised four steps: (1) a C/3 charge to 4.4 V, (2) 0.5 h constant-voltage (CV) hold at 4.4 V, (3) 0.5 h rest ( $I = 0$  mA), and (4) a C/3 discharge to 2.5 V. As seen in Fig. 3(a), the electrochemical data are qualitatively comparable. The charge and discharge profiles evolve like those discussed in Sec. I, displaying the same signatures of cell-impedance

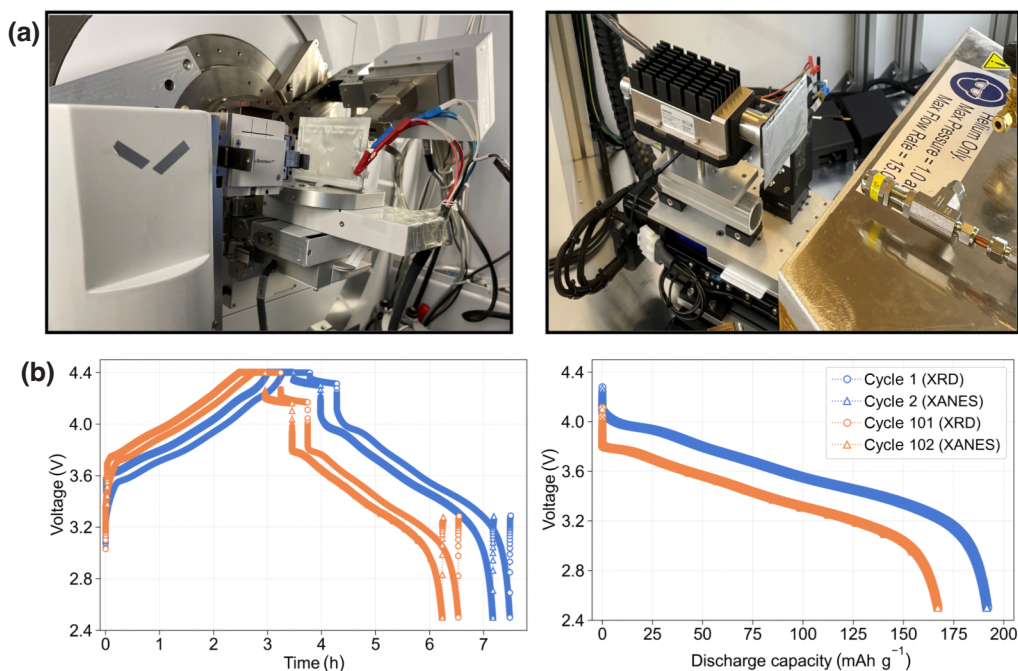


FIG. 3. (a) Photographs of the pilot-line cell on the diffractometer (left) and spectrometer (right). (b) Left: the voltage-time profile during the *operando* XRD and Ni K-edge XANES experiments of the pilot-line cells. Right: the discharge capacity obtained during the four *operando* cycles.

growth and electrode slippage [54]. Discharge capacities obtained in consecutive *operando* experiments are highly comparable, indicating that cycles 2 and 102 (XANES) are analogous to the preceding cycles. Figure S4 in the Supplemental Material [73] shows data from the CV and rest steps, respectively. Note that the CV hold was restricted by time and not a current limit. The current required to maintain the voltage increases by approximately a factor of 2.4 after 100 cycles. This increase is due to the growth of the rock-salt surface layer on the cathode kinetically hindering delithiation during the charging step [19]. The CV hold helps to overcome this, facilitating further delithiation. The effect of cathode-surface-layer build-up is further evidenced by the voltage evolution during the rest step [Fig. S4(b) in the Supplemental Material [73]], where the voltage drop increases by approximately 0.15 V after 100 cycles, thereby corroborating the EIS data. Thus, the electrochemical data from the *operando* experiments conforms to Sec. I, indicating that the observed capacity

fade is linked to the increased cell impedance due to cathode surface reconstruction. The effects of this on their bulk structure can be tracked through the x-ray experiments.

Figures 4(a) and 4(b) show the *operando* XRD and Ni K-edge XANES data, respectively. XRD data were only collected between 1.2 and 2.75  $\text{\AA}^{-1}$  in  $Q$  (the scattering vector), i.e., 7–18° scattering angles (Mo  $K\alpha$ ), as they contain sufficient information to track the structural evolutions of both electrodes. The *operando* XRD data resemble those from the literature and generally reveal a solid-solution behavior for the NMC cathode [19,20,57]. The 003 reflection initially shifts to lower scattering vectors and/or angles, followed by a comparatively rapid shift to higher values. On the other hand, the 101 reflection shows a monotonic shift toward higher scattering vectors initially, after which it moves back toward its original position. The graphite 002 reflection also behaves as expected, shifting toward lower scattering vectors and splitting

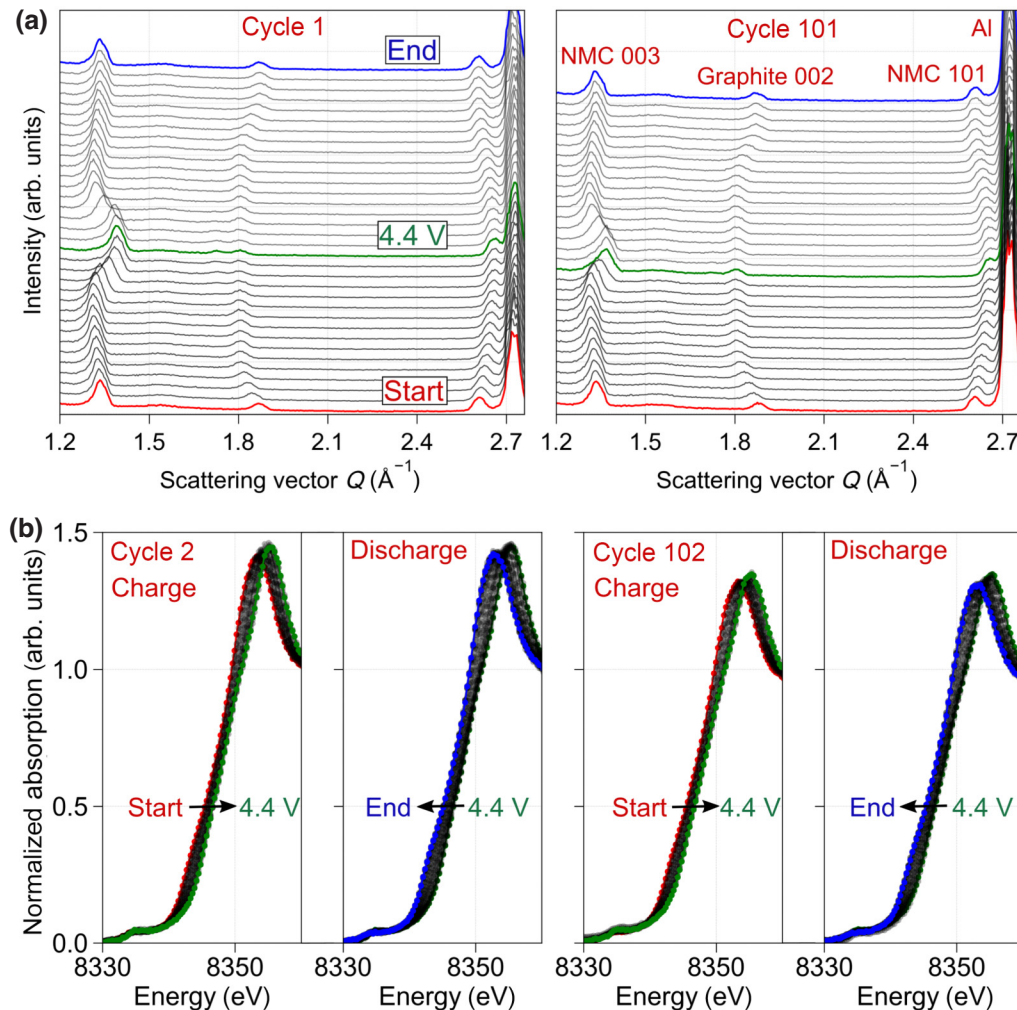


FIG. 4. (a) The *operando* XRD data (offset in  $y$ ) with the peaks highlighted, as are the scans at the start, top of charge (4.4 V), and end. (b) The *operando* Ni K-edge XANES data from the second and 102nd cycles separated into the charge and discharge steps.

into  $\text{LiC}_{12}$  and  $\text{LiC}_6$  phases at the top of charge before returning to its original state at discharge (see Fig. S5 in the Supplemental Material [73]). Higher-quality *ex situ* XRD data (see Fig. S6 in the Supplemental Material [73]) of the cells collected before and after the *operando* experiments show remarkable reversibility in the electrode-structure evolution with no noticeable phase transformations, even under the current cycling conditions. The Ni K-edge XANES data, shown in Fig. 4(b), also show the expected edge shifts toward higher and lower energies, upon charge and discharge, respectively. Normalized data across the full energy range are shown in Fig. S8 in the Supplemental Material [73]. However, although the *operando* x-ray data look qualitatively comparable, it is evident that the extent of the bulk-electrode-structure changes varies over the course of cycling.

### C. Quantitative analysis of the *operando* data

The evolution of the  $R\bar{3}m$  unit-cell parameters and the Ni K-edge half-height (half of the normalized edge height) of the NMC cathode, with their corresponding *operando* electrochemical data, are shown in Fig. 5. The  $c$  lattice parameter initially increases before collapsing at higher states of charge—the so-called “ $c$ -lattice” collapse. The  $a$  lattice parameter, on the other hand, monotonically decreases before plateauing toward the end of charge. During both XRD experiments, the same kind of changes, albeit to different degrees, are observed. In

cycle 1,  $c$  and  $a$  contract by approximately 4% and 2%, respectively, during charging before recovering completely upon discharge. During cycle 101, the  $c$ -lattice-parameter contraction halves (approximately 2%), whereas that of the  $a$  lattice parameter remains comparable to that in cycle 1. The corresponding unit-cell volume changes are shown in Fig. S7 in the Supplemental Material [73] and essentially show the same trend as that of the  $c$  lattice parameter. This reduction in the extent of the  $c$  lattice parameter and the unit-cell volume contraction during charge is indicative of a decrease in bulk delithiation and has been observed previously [19]. As will be discussed later, this phenomenon stems from the sluggish  $\text{Li}^+$  kinetics due to the increased cell impedance after 100 C/3 cycles and is also reflected in the graphite-structure evolution as the reduction in the “Li-rich”  $\text{LiC}_6$  phase formation after 100 cycles (see Fig. S7 in the Supplemental Material [73]). Further corroboration is obtained from the *operando* XANES data. In Ni-rich NMC cathodes, Ni exists in mixed II-III oxidation states and is the major participant in the charge-compensation reaction [58]. By tracking the edge half-height, an indirect measure of the bulk Ni oxidation state, it is clear that Ni does not continuously oxidize during the charge; nor does it reach the formal IV oxidation state [59]. As seen in Fig. 5(d), the half-height monotonically increases by about 1.2 eV during the charge step of both experiments before plateauing and remaining largely invariant during the subsequent

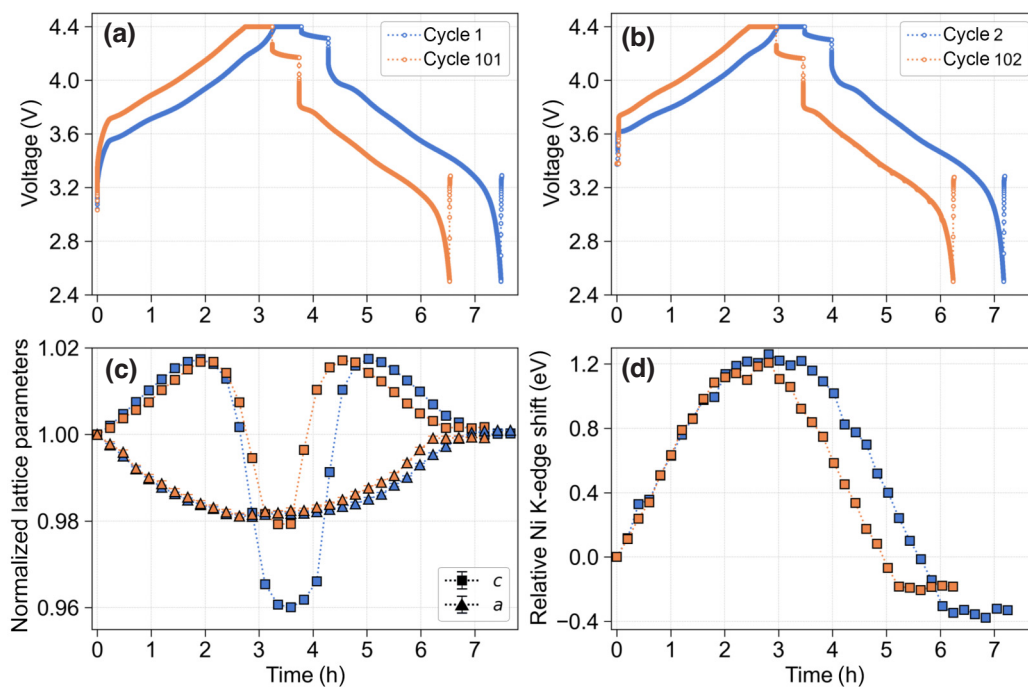


FIG. 5. Voltage-time profiles of the pilot-line cell during the *operando* (a) XRD and (b) XANES experiments. (c) The normalized evolution of the lattice parameters obtained from Pawley fitting of an  $R\bar{3}m$  unit cell to the *operando* diffraction data. (d) The relative shift of the Ni K-edge obtained from the half-height of the normalized XANES data.



CV and rest steps. As per conventional ionic models, this represents the simultaneous stop and start of bulk Ni and O oxidation, respectively. However, recent studies question this ionic approximation and, therefore, interpreting the Ni K-edge half-height plateauing at high voltages as “O-redox” activation is overly simplistic, because of the strong Ni—O covalency in such materials [58,60,61]. Upon discharge, the half-height drops below the starting value, indicating Ni reduction close to II states. This may result in increased proclivity to form the aforementioned rock-salt NiO-like cathode surface layer that increases the overall cell impedance [34,35]. The extent of Ni reduction also reduces after 100 cycles, which indicates reduced cathode lithiation as discussed previously. Furthermore, Ni reduction ceases at approximately 3.5 and 3.3 V during the postformation and 100-cycle experiments, respectively. However, approximately 70 and 50 mAh g<sup>-1</sup> capacities are obtained at these stages, respectively, indicating that lithiation may likely be compensated by (possibly deleterious) factors other than bulk Ni reduction, such as parasitic electrode-electrolyte reactions. Although reported to be comparatively minor for single-crystalline morphologies, TM dissolution to the anode (crosstalk) may also play a role, considering the wide operating-voltage windows and higher cycling temperature used in this study [13,34,37,49]. The aforementioned cathode surface reconstruction to rock-salt phases, due to its role in impeding the

Li<sup>+</sup> kinetics, can also form “fatigued” NMC phases in the bulk over the course of cycling [18–20].

The *operando* XRD data together with the postmortem data from discharged cathodes provide insight into the formation of fatigued phases. These phases are generally described as bulk rhombohedral phases with reduced electrochemical activity that are formed with prolonged cycling. Their exact origin remains subject to debate, with both kinetically limited (de)lithiation [15,19] and surface-bulk interfacial strain [20] suggested as causal candidates. In diffraction data, it is seen as the broadening and/or splitting of the parent NMC reflections, as in Fig. 6(a), where the NMC 003 reflection at the fully charged state significantly broadens after 100 cycles. Thus, the structural fatigue grows in the single-crystalline NMC cathode over the course of cycling. Note that the Li<sup>+</sup> kinetics in such NMC cathodes can also suffer due to the longer diffusion paths in the large(r) particles and lead to spatial inhomogeneities in the Li<sup>+</sup> concentration and internal stresses [15]. This produces the same broadening effect on the 003 reflection XRD data. However, the limited time and angular resolution of the *operando* data precludes further analysis of the fatigued phase. Nevertheless, it is evident that the cathode-structure evolution is remarkably reversible, even after 100 cycles under the conditions used in this work. To investigate this reversibility further and compare the fatigued phase formation in the pilot-line and

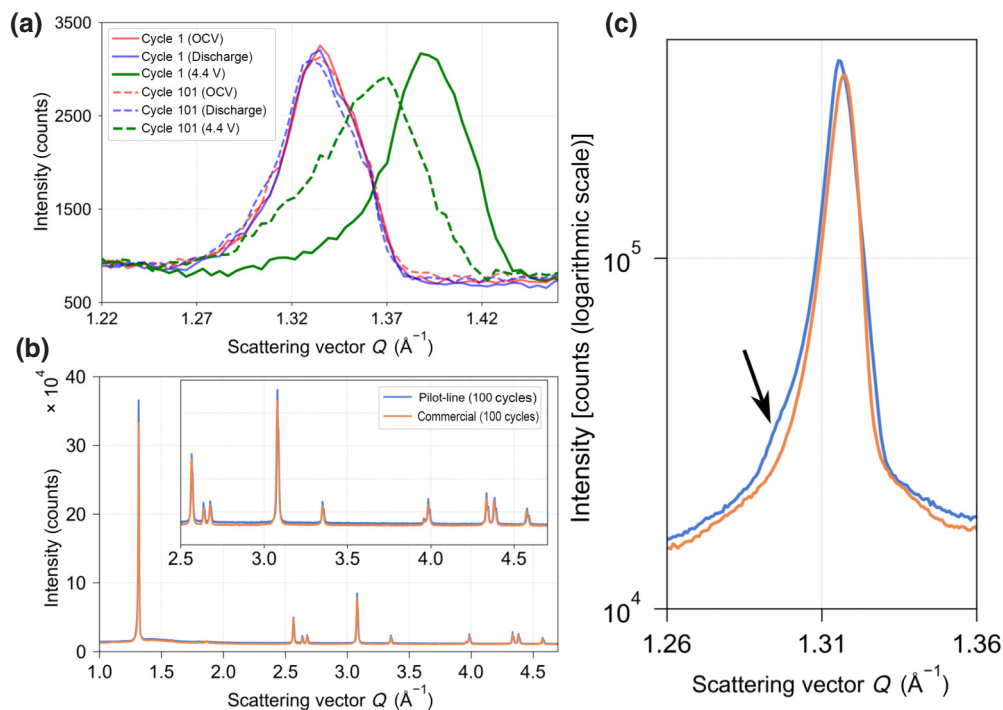


FIG. 6. (a) The NMC 003 reflection from the *operando* XRD data at the OCV (red), fully charged (green), and discharged (blue) conditions. (b) *Ex situ* XRD patterns of the discharged electrodes from the two cells after 100 cycles. (c) The 003 reflection from (b) replotted in logarithmic scale to highlight the possible fatigue phase (using the arrow).



commercial cathodes, higher-resolution *ex situ* XRD data were collected in the discharged state after 100 cycles. Fitting an  $R\bar{3}m$  unit cell to the data reveals that after 100 cycles, the  $c$  lattice parameter increases, whereas the  $a$  lattice parameter decreases (see Table S2 and Fig. S9 in the Supplemental Material [73]). This trend is seen in both the pilot-line and commercial cathodes and has been observed elsewhere [21]. From Fig. 6(b), it is evident that both cathodes show a high degree of reversibility, without any new peaks compared to their pristine state [Fig. 1(d)]. The data are also highly comparable in terms of the overall peak widths, indicating no significant microstructural changes. However, replotting the intensity in a logarithmic scale [Fig. 6(c)] reveals a shoulder toward the left of the 003 reflection ( $\sim 1.29 \text{ \AA}^{-1}$ ) in the pilot-line cathode data that is not visible in the commercial one, suggesting traces of the fatigued phase. Although weak, the presence of this phase

only in the pilot-line cathode and not the surface-modified commercial one is an indication that its formation might be dependent on the extent of cathode surface reconstruction and its impact on the kinetics of delithiation. However, further longer-duration investigations with varied experimental conditions are necessary to fully understand the origins and growth of the fatigued phase. Nevertheless, it is also important that the extent of cathode particle cracking be investigated before conclusions are drawn.

Cathode particle cracking was investigated on post-mortem (discharged) samples using scanning electron and x-ray microscopy. Figure 7(a) shows wide-cross-section SEM images of the pilot-line cathode after two and 102 cycles, respectively. No significant cracks or fractures are observed. Although expected [6–12,15], it is still remarkable considering the cycling conditions used in this work—even more so as the electrodes were machine

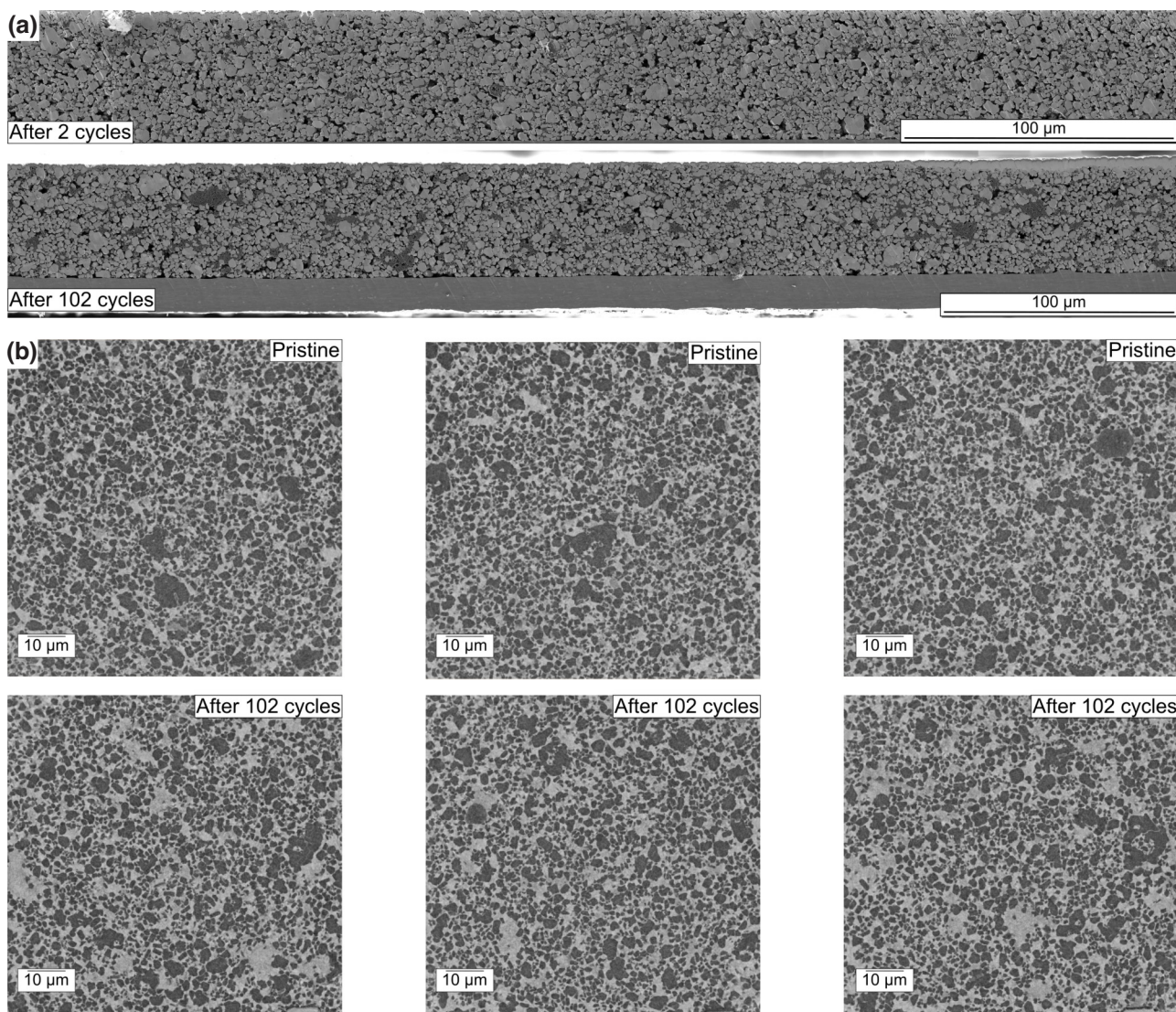


FIG. 7. (a) Cross-section SEM and (b) selected HXCT slices of the cycled pilot-line cathodes. The SEM images from the pristine electrodes are provided in the Supplemental Material [73].

fabricated under industry-relevant conditions. Additionally, an increased degree of carbon segregation (darker regions) is seen in the 100-cycle electrode. It is currently uncertain whether this is a consequence of the electrochemical cycling or imperfect electrode slurry mixing. Focused-ion-beam–scanning-electron-microscopy (FIB-SEM) tomography was performed on the samples to exploit the high resolution over a large field of view, as observed in the videos in the Supplemental Material [73] after 2 and 102 cycles. However, the destructive nature of this characterization can create defects or artifacts that were not present in the original sample. While the images showed no significant evidence of cracking, nondestructive holographic x-ray computed tomography (HXCT) [58] was employed with a pixel size of 40 nm to observe particles *in situ* and corroborate the SEM findings. Selected slices can be seen in Fig. 7(b), with the videos in the Supplemental Material [73] translating the entire cathode volume. Once again, no significant evidence of cracking is seen, confirming the ability of the cathodes to resist cracking and/or fracture after 100 cycles. Note that the absence of cracking is also consistent with chemomechanical simulation studies of stress generation in single-crystalline NMC811 particles [62]. Similarly, no signs of cracking are found in the cycled commercial-cell cathodes (see the Supplemental Material [73]). Therefore, particle cracking may be ruled out as a driver of electrochemical performance degradation in these cathodes. As neither cathode shows

any signs of cracking, irrespective of surface modifications, it may be understood that cathode surface modifications do not play a role in influencing the cracking behavior of single-crystalline Ni-rich cathodes. The data-collection and -analysis methodology of the SEM data, together with higher-resolution images and/or videos, are also included in the Supplemental Material [73]. Taken together, the x-ray and electrochemical data suggest that the increasing cell impedance due to the cathode surface reconstruction and the consequent worsening of the  $\text{Li}^+$  kinetics are the primary modes of capacity fade in the pilot-line cells, even when operated under such harsh conditions.

#### D. Reversible and irreversible capacity loss in pilot-line cells

Based on the results discussed thus far, the pilot-line cells show a steady loss in capacity over 100  $C/3$  cycles, which does not originate from structural transformations or cathode particle cracking. The nature of this capacity fade was further investigated using another pilot-line cell cycled 100 times under the same conditions, with two  $C/20$  diagnostic cycles at the end. The discharge-capacity values from this cell are shown in Fig. 8(a). As seen, the cell discharge capacity is dependent on the cycling rate, with both the formation and diagnostic cycles showing notably higher capacities than the regular  $C/3$  cycles. Between the second formation and the first  $C/3$  cycles, a rapid loss

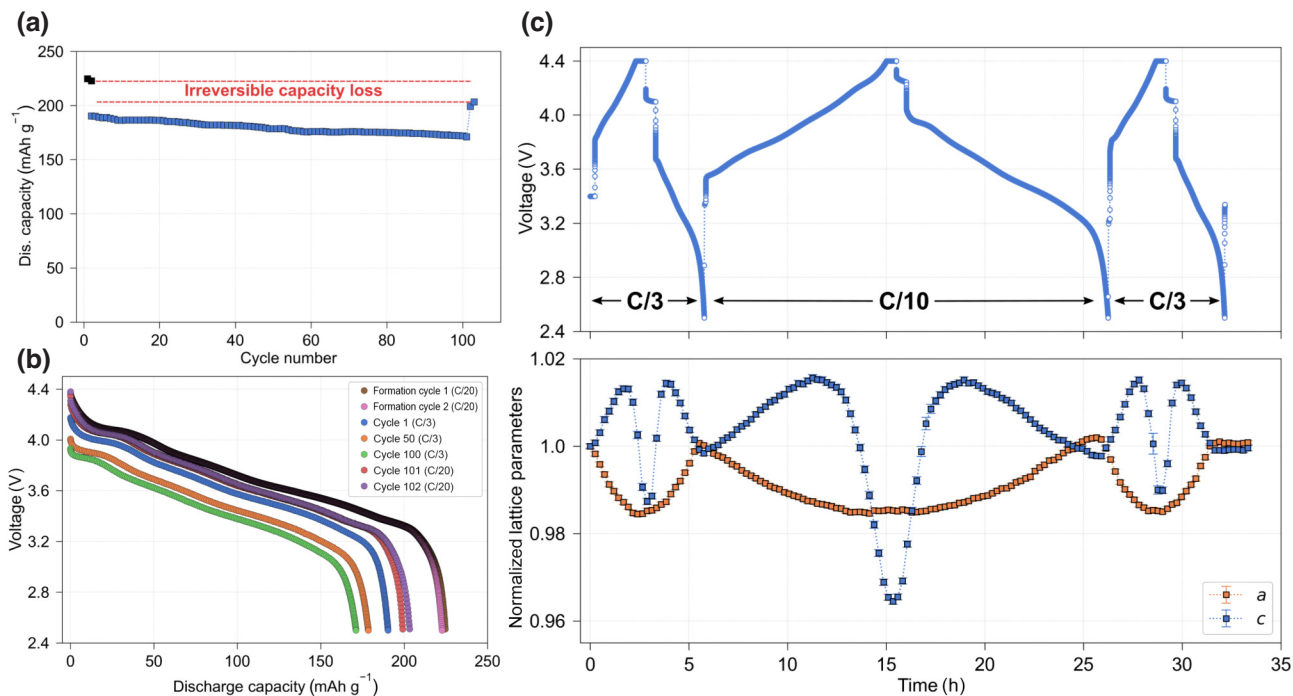


FIG. 8. (a) The discharge capacity plotted as a function of the cycle number. The black dots correspond to the capacity from the formation cycles. (b) Voltage–discharge capacity plots of the pilot-line cell from selected cycles. (c) The voltage–time profile and the corresponding refined evolution of the NMC811 unit-cell parameters of the pilot-line cell after 100+ cycles from the *operando* XRD experiment.



of  $32.4 \text{ mAh g}^{-1}$  is seen, which may be understood to be dependent on the slower  $\text{Li}^+$  kinetics at the C/3 rate. Between the first and 100th C/3 cycles, the capacity loss is  $19.2 \text{ mAh g}^{-1}$  ( $\approx 10\%$ ), similar to that in Fig. 2(b). In the following two diagnostic cycles, the capacities increase by 28 and  $32.2 \text{ mAh g}^{-1}$ , respectively, illustrating that the capacity lost during the 100 C/3 cycles is partially reversible. However, between the second formation and diagnostic cycles,  $19.4 \text{ mAh g}^{-1}$  capacity is lost, corresponding to the amount of capacity irreversibly lost due to the consumption of  $\text{Li}^+$  species during SEI growth [highlighted in Fig. 8(a)]. Therefore, as mentioned previously, the pilot-line cells lose capacity in both reversible and irreversible manners. As seen in Fig. 8(b), there is a distinctive decrease in the cell potential during the 100 C/3 discharge cycles, which is notably lower than during the C/20 cycles. This is primarily dependent on the cathode surface reconstruction into dense rock-salt layers, which significantly impedes the  $\text{Li}^+$  kinetics, as reflected in the EIS data shown in Fig. 2(d). The slower cycling rate can overcome the effects of the increased impedance and, hence, significantly recover the capacity lost during the faster C/3 cycle.

To confirm that the increased capacity during the slower diagnostic cycle originates truly from bulk (de)lithiation, an *operando* XRD study of a similarly aged pilot-line cell during three continuous cycles at C/3, C/10, and C/3 rates was carried out. In Fig. 8(c), the cell voltage profile is plotted with the refined NMC cathode  $R\bar{3}m$  unit-cell parameters. The full XRD data from the *operando* experiment are shown in Fig. S10 in the Supplemental Material [73]. As seen, the second C/10 cycle provides a higher capacity than the C/3 cycles ( $\approx 34.5 \text{ mAh g}^{-1}$ ; see Fig. S11 in the Supplemental Material [73]). The corresponding increase in the  $c$ -lattice-parameter drop shows that the higher C/10 capacity originates from bulk cathode (de)lithiation and not from other factors such as structural phase transformations or electrolyte oxidation. Furthermore, the Li-rich  $\text{LiC}_6$  phase is also visible, although weakly, in the XRD data only during the C/10 cycle (see Fig. S12 in the Supplemental Material [73]), which further confirms the increased (de)lithiation of the electrodes. The NMC  $a$  lattice parameter, such as that in Fig. 5(c), does not show any variation based on the cycling rate. As shown in Fig. S13 in the Supplemental Material [73], the NMC 003 reflection at the top of the charge from the *operando* XRD data is comparatively sharper in the C/10 cycle than in the C/3 cycles, suggesting reduced fatigue-phase formation in the C/10 cycle. The CV step data from the *operando* experiment (Fig. S14 in the Supplemental Material [73]) shows that the current needed to hold the cell at 4.4 V is higher in the C/3 cycles than in the C/10 cycle. This is because the faster C/3 cycling due to the slower  $\text{Li}^+$  diffusion at the C/3 rate leads to a more heterogeneous state of delithiation after charging. Consequently, a higher

current is required to maintain the 4.4-V hold. This is also reflected in the voltage drop during the rest that follows the CV step (Fig. S14 in the Supplemental Material [73]). The drop is comparatively smaller for the C/10 cycle, as the slower cycling reduces the overpotential developed in the cell during charging. Note that the capacity fade from the *operando* experiment should not be directly compared to the regular electrochemical cycling, as the former was performed under ambient conditions without stack pressure. Taken together, the capacity fade in the pilot-line cell cycled 100 times at C/3 rate between 2.5–4.4 V at  $40^\circ\text{C}$  is primarily due to the increased cell impedance and the consequent sluggish  $\text{Li}^+$  kinetics in the cathode, which can be recovered through slower cycling. Furthermore, mitigating the growth of the cathode surface layers through surface passivation [as in the commercial cells via Al surface doping; see Fig. 2(b)] or electrolyte additives, is expected to improve the cycling-rate-dependent capacity fade.

### III. CONCLUSIONS

The effects of long-term electrochemical cycling under stressful conditions (2.5–4.4 V and  $40^\circ\text{C}$  at C/3 for 100 cycles) on single-crystalline Ni-rich cathodes in pilot-line-built A7 full cells were investigated using *operando* x-ray and postmortem microscopy studies. The primary origin of capacity fade ( $\approx 10\%$ ) when cycled under such conditions was the sluggish  $\text{Li}^+$  kinetics due to the formation of the resistive rock-salt surface layer on the cathode. This layer, formed as a consequence of the O-loss-induced surface reconstruction, impedes  $\text{Li}^+$  diffusion and increases cell impedance. However, this capacity loss is reversible and may be recovered through slower cycling, as illustrated by the C/20 diagnostic cycles at the end. However, the diagnostic cycle is not able to recover all the lost capacity, indicating that some of it is irreversibly lost, presumably due to the (anode) SEI layer growth. Structurally, the pilot-line cell cathode shows fatigued phases in the cathode bulk after 100 cycles at high states of charge. Although it was not possible to ascertain their origins, the XRD data revealed that all cycling-induced transformations in the cathode were largely reversible. However, traces of the fatigued phase were found in the discharged pilot-line cell cathode, suggesting that surface passivation, as found in the commercial-cell cathodes, might be a pathway to suppress them and counter this mode of degradation. Furthermore, neither cathode showed any significant degree of cracking despite the extreme anisotropic structural evolution of the cathode particles. Going forward, longer-term studies ( $>100$ s of cycles) are key to understanding and quantifying degradation in Li-ion battery cells. If this knowledge is to be used toward practical performance gains, the studies must be performed in conditions as close to the

real world as is reasonably possible. Furthermore, caution must be exercised when extrapolating and comparing individual studies due to the differences in their experimental and metrological parameters. As per the recent articles highlighting the existing academia-industry disconnect in the battery-research community [17,40,42], fundamental investigations of degradation pathways under industry-relevant conditions, such as the current study, are vital to bring economically viable cell chemistries closer to commercialization.

## IV. EXPERIMENTAL DETAILS

### A. Pilot-line pouch-cell fabrication and assembly

The pouch-cell assembly was performed using the established standard operating procedures for single-layered A7 pouch cells on the WMG battery scale-up pilot line (TRL-5) in a dry room (dew point of  $-45^{\circ}\text{C}$ ). The cathode was prepared with a mix of  $\text{LiNi}_{0.8}\text{Mn}_{0.1}\text{Co}_{0.1}\text{O}_2$  (NMC811, 95.5%), PVDF (2.5%), and conductive carbon additive (2%) using a Bühler high-torque mixer and coated onto a 15- $\mu\text{m}$ -thick aluminum foil (Avocet Steel Strip Ltd.) with a target thickness of 45  $\mu\text{m}$ . The anode sheet was prepared similarly with a graphite (BTR V-H)–carboxymethyl cellulose (CMC, Ashland BVH8)–styrene-butadiene rubber (Zeon BM451)–carbon (Imerys C45) mix of 95.5:1.5:2.25:1 (wt.%) and coated onto a 10.2- $\mu\text{m}$ -thick copper foil (Avocet Steel Strip Ltd.). The cathode and anode coat weights were approximately 12.3 and 10.8  $\text{mg cm}^{-2}$ , respectively. The cathode was calendared to a press density of 2.7 and the anode to 1.4. Both electrodes were cut using an A7 cutter as per the required sizes. The cathode surface area was 33.22  $\text{cm}^2$ , with the anode surface area being 35  $\text{cm}^2$ . Following this, the current-collector tabs were ultrasonically welded onto the electrodes. External current collector tags (cathode, Al; anode, Ni-coated Cu) were then ultrasonically welded onto the electrodes. Following this, the two electrodes were stacked together, separated by a Celgard 2325 25- $\mu\text{m}$  trilayer microporous membrane. The anode-separator-cathode assembly was then packed into an aluminum-laminated pouch cell and filled with 1 g of commercial “LP57” electrolyte, i.e., 1 M lithium hexafluorophosphate ( $\text{LiPF}_6$ ) in ethylene carbonate (EC) and ethyl methyl carbonate (EMC) (3:7 vol.%) with a 2% vinylene carbonate (VC) additive (Solvionic) by weight, and sealed under vacuum (280 mbar). The pouch cells were balanced with a N:P ratio (negative: positive electrode capacity ratio) of approximately 1.4. The pouch cells had an approximate areal capacity of 2.1  $\text{mAh cm}^{-2}$ .

For the *operando* studies after formation and 100 cycles, two different pouch cells were used. For the postformation experiments, the cathode coating was performed at the WMG pilot line using commercially sourced powder following the above procedure, whereas for the 100-cycles

experiments, the cathode coating was provided by an industrial partner and prepared using the same powder. The phase purity of the NMC811 powder was confirmed using Rietveld analysis [63,64] of XRD data and inductively coupled plasma optical emission spectroscopy (ICP-OES). The results from the diffraction analysis are included in Fig. S15 and Table S3 in the Supplemental Material [73]. The average composition as per the ICP-OES experiment was found to be  $\text{Li}_{1.01}\text{Ni}_{0.81}\text{Mn}_{0.06}\text{Co}_{0.11}\text{O}_2$ .

### B. Commercial cells

Dry 402035-type multilayer pouch cells with calendared double-sided (proprietary) surface-modified single-crystalline Ni-rich NMC cathodes and graphite anodes were obtained from LiFun Technology Corporation Ltd. The cathode had an active material loading of 16.71  $\text{mg cm}^{-2}$  (95.5%), with an active area of 76.96  $\text{cm}^2$ . The corresponding active material loading of the anode was 11.3  $\text{mg cm}^{-2}$  (94.8%). The cathode and anode press densities were 3.3 and 1.5  $\text{g cm}^{-3}$ , respectively. The cells were balanced to 4.3 V with an N:P ratio of 1.17. Before electrolyte filling, the cells were cut open and vacuum dried at  $100^{\circ}\text{C}$  overnight. Following this, the cells were filled in the dry room with 1.1 g of LP57 electrolyte and then resealed under vacuum.

### C. Electrochemistry

Both the pilot-line and commercial cells were subjected to the same electrochemical cycling protocols, detailed below. A Maccor 4000 series cyler was used for electrochemical cycling. Initially, the cells were held at 1.5 V for 20 h at  $40^{\circ}\text{C}$  in a climate chamber to ensure homogeneous electrolyte wetting of the electrode. Following this, the cells were subjected to two formation cycles under galvanostatic conditions at approximately C/20 ( $1\text{C} = 200 \text{ mAh g}^{-1}$ ) between 2.5 and 4.4 V. The commercial cells were then degassed and vacuum sealed, whereas the pilot-line cells were not degassed as the gas evolution was minimal, if not negligible. Both cells were then cycled in a constant current–constant voltage (CCCV) mode during charge and CC mode during discharge, with a C rate of C/3 at  $40^{\circ}\text{C}$  between 2.5 and 4.4 V for 100 cycles. The CV step was limited using a minimum current value of C/30. Three cells were cycled to ensure reproducibility. Note that due to an error with the Maccor cyler programming, the CV data steps were not properly recorded for the pilot-line cells (for more information, see Sec. S1 in the Supplemental Material [73]). Potentiostatic electrochemical impedance spectroscopy (PEIS) of the cells was measured after formation and 100 cycles using a Biologic VMP3 potentiostat. Before the measurement, the cells were charged to 3.8 V at C/20. EIS data were collected at 3.8 V at  $25^{\circ}\text{C}$ , with an amplitude of 10 mV between 100 kHz and 10 mHz. EIS measurements



on the pilot-line cells were performed using the same protocol but using a Biologic SP150 potentiostat prior to the *operando* XRD experiment (cycle 1 and 101).

For postmortem *ex situ* XRD and SEM measurements, cells were disassembled in an argon glove box (MBraun) ( $\text{O}_2$  and  $\text{H}_2\text{O} < 1$  ppm) after cycling to the desired points and discharging to 2.5 V. The extracted electrodes were washed with dimethyl carbonate (DMC, anhydrous  $\geq 99\%$  purity, Sigma-Aldrich) to remove electrolyte residue and then dried in the glove box. The dried electrodes were transferred into the air-tight sample holders for subsequent studies.

#### D. *Operando* and *ex situ* x-ray experiments

*Operando* x-ray experiments were performed galvanostatically between 2.5 and 4.4 V at a rate of C/3 using a Biologic SP150 potentiostat under ambient room-temperature conditions. Each experiment consisted of a charge followed by discharge, with CV and rest ( $I = 0$  mA) steps lasting 0.5 h each. The *operando* experiments were performed after formation and 100 cycles using two separate pilot-line cells with near-identical specifications. In each case, the diffraction (cycles 1 and 101) and spectroscopy (cycles 2 and 102) experiments were performed back to back. As mentioned before, the EIS measurements were performed prior to the diffraction experiments. Following this, the cells were discharged to 2.5 V at C/20 before the *operando* experiments started. A rest step of 1 min was included in the beginning to coordinate the start of the cycling and x-ray experiments. The C/3-C/10-C/3 rate-test *operando* experiment on the aged cell was also performed using the same protocols but without the EIS measurement. The electrochemical and *operando* data were synchronized using time.

*Operando* XRD was performed on a Malvern Panalytical Empyrean diffractometer (60 kV, 40 mA) with  $\text{MoK}\alpha$  radiation ( $K\alpha_1 = 0.709319$  Å,  $K\alpha_2 = 0.713609$  Å) in transmission using a XYZ stage. On the incident-beam side, a  $\text{ZrCuK}\beta$  filter, a Soller slit (0.02 rad), a divergence slit (0.5°), and an antiscatter slit (0.25°) were used. Antiscatter (5 mm) and Soller (0.04 rad) slits were used on the diffracted-beam side. Data were collected between 7.5° and 18°, using a step size of  $\sim 0.028^\circ$  ( $2\theta$ ) with a counting time of  $\sim 530$  s per step, by means of a GaliPIX3D detector (active length of 4.996°) in scanning mode. Accounting for the time for the instrument to reconfigure after the end of a scan, the total duration of each scan may be approximated to 15 min. Additionally, higher-resolution diffraction data were collected before and after the *operando* measurement using a 0.02-rad diffracted-beam-side Soller slit between 7° and 32° ( $2\theta$ ) with a step size of  $\sim 0.028^\circ$  and time per step of  $\sim 980$  s ( $\sim 1$  h total time). Note that the scan before the start was collected at 3.8 V, just before the EIS measurement. (*Ex situ*) XRD measurements of

the cathodes and the NMC811 powder were carried out using a Malvern Panalytical Aeris diffractometer (40 kV, 15 mA) with  $\text{CuK}\alpha$  radiation in Bragg-Brentano mode. The incident beam side had a  $\text{NiCuK}\beta$  filter, a Soller slit (0.04 rad), a divergence slit (0.25°), and a 13-mm x-ray mask. Antiscatter (9 mm) and Soller (0.04 rad) slits were used on the diffracted-beam side. Data from the cycled electrodes, protected from air exposure using a Kapton film, were collected using a zero-background Si holder between 10° and 75° ( $2\theta$ ) while spinning. The measurements were made with a step size of about 0.01° and a time per step of 150 s, using a PIXcellD-Medipix3 detector. Pawley [65] refinement analysis of the XRD data was performed using the TOPAS-ACADEMIC (v. 7) [66] software.

*Operando* Ni K-edge x-ray absorption near-edge structure (XANES) measurements were performed using an easyXAFS300+ spectrometer in transmission mode [67]. The desired energy range of 8300–8800 eV was accessed using an Si (551) spherically bent crystal analyzer. X-ray air scattering was minimized using a helium gas chamber. To optimize the absorption edge data, the XANES data collection was carried out in three parts: (1) preedge, 8286–8315 eV (2-eV step size and 1-s time per step); (2) edge, 8315–8380 eV (0.3-eV step size and 2.5-s time per step); and (3) postedge, 8380–8800 eV (5-eV step size and 2-s time per step). Therefore, the total measurement time approximates to 14 min per scan. Each data set was dead-time corrected, normalized (using the empty beam), and energy calibrated using reference Ni foil with the instrument software. The subsequent preedge background subtraction and postedge normalization were carried out using the ATHENA software package [68]. For each *operando* data set, the preedge and normalization range values were optimized for the first scan and then fixed for the remaining scans. A normalization order of 2 was used throughout. The half-height of the normalized spectra, i.e., the energy value at which the intensity is 0.5, was calculated using the OriginPro 2022 software.

#### E. XRD data analysis

The NMC811 phase in the *operando* XRD data was analyzed through sequential Pawley refinements [65] using an  $R\bar{3}m$  unit cell with starting  $a$  and  $c$  lattice parameters of 2.87 and 14.2 Å, respectively. The refinements were performed using a fourth-degree polynomial background function and a Thompson-Cox-Hastings modified pseudo-Voigt peak-shape function. An aluminum phase ( $a = 4.043$  Å,  $Fm\bar{3}m$ ) was also included. Only the 003 and 101 reflections of the NMC811 phase were used for the refinement due to the overlap of the 006 and 102 reflections with the Al 111 reflection. Specimen displacement was not included in the refinements but the invariance in the position of the cell over the course of the experiment

was tracked indirectly by refining the Al lattice parameter, which did not change significantly. The portion of the data with the graphite peaks were excluded in these refinements. The graphite phase evolution was tracked with sequential peak fitting using two peaks, with their positions restricted to the ranges covered by the LiC<sub>12</sub> and LiC<sub>6</sub> phases. The peak position, intensity, and shape (Thompson-Cox-Hastings modified pseudo-Voigt) parameters were refined. A second-order polynomial function was used to model the background. The integrated peak-intensity variations were used to track the evolution of the graphite phases.

*Ex situ* XRD data of the NMC811 electrodes were also analyzed using the Pawley method. To account for the diffuse background from the Kapton file, the background points were manually selected and included in the refinements. The symmetric broadening of the peaks was modeled using the Thompson-Cox-Hastings modified pseudo-Voigt peak-shape function. The peak shape asymmetry due to axial divergence was modeled using the SIMPLE\_AXIAL\_MODEL function in the software. The specimen displacement was also refined. Rietveld refinement of the pristine NMC811 powder was also carried out using the same parameters, with the addition of the scale factor, the *z* coordinate of the oxygen atom, and the occupancies of the Li and Ni atoms. The occupancies of the Mn and Co atoms were fixed to 0.1 and not refined. The isotropic atomic displacement parameter ( $B_{\text{iso}}$ ) was fixed to 0.5 for all atoms and not refined. Definitions of the various refinement functions and the refinement metrics can be found in the TOPAS manual. The refined values are included with the raw data.

### F. Scanning electron microscopy

Cathode cross sections for SEM were prepared by Ar broad-beam ion milling (BBIM). Pieces of cathode were prepared in an Ar glove box and transferred to an Hitachi IM4000Plus ion-milling system equipped with an air-protection unit. Cross-section milling was performed at 6 kV for 2.5 h with 40° stage rocking. The sample was then transferred back to a glove box using the IM4000Plus air-protection capsule. The cross sections were then transferred without air exposure to a Thermo Fisher Scientific Scios Dualbeam using the CleanConnect inert gas transfer system [69] for imaging. Secondary-electron (SE) images were acquired using an accelerating voltage and a beam current of 2 kV and 100 pA, respectively. Wide-area SEM montage images were acquired and stitched using the Thermo Fisher Scientific MAPS software. FIB-SEM tomography was performed using a Thermo Scientific Scios Dualbeam system. The wide-area cross sections were first prepared by Ar BBIM as outlined above. The prepared cross sections were then transferred to the Dualbeam system using the CleanConnect inert gas transfer system [1].

A platinum protective layer was deposited close to the edge of the prepared cross section. FIB rough milling was performed using a 30 kV–50 nA Ga beam, followed by cleaning with a 30 kV–15 nA Ga beam to leave a volume approximately  $40 \times 40 \times 40 \mu\text{m}^3$  in size. Tomographic slicing was performed using a 30 kV–5 nA Ga beam to cut slices with a nominal thickness of 50 nm. SE SEM images were acquired after each slice using 2 kV–100 pA beam conditions. The FIB-SEM tomography data were aligned using the DRAGONFLY software [70]. A pyramid alignment followed by linear drift compensation was used to align the image slices. The scale bar in the tomography videos corresponds to 10  $\mu\text{m}$ .

### G. Holographic x-ray computed tomography

The discharged cathode samples were prepared by extracting a 100- $\mu\text{m}^3$  cube using a Ga FIB (similar to the SEM cross sections) and mounted on a carbon rod sat within a pin, suitable for the positioning system at the ID16A beam line at ESRF, France [71]. The x-ray beam line is highly coherent, with a 185-m source-to-detector distance, focused to a 12-nm spot size. To perform the tomography experiment, the sample was placed between the spot and a  $4096 \times 4096$  pixel detector while operating at 33.6 keV. This was then rotated through 180°, with 1500 projections recorded at each of four different magnifications [72]. An iterative holographic phase-retrieval method was applied to each acquisition, followed by back projection to generate the final image volume, with a final pixel size of 40 nm across a  $128.64 \mu\text{m} \times 128.64 \mu\text{m} \times 81.92 \mu\text{m}$  volume. The preparation of the final images and the analysis was performed in the AVIZO (Thermo Fisher Scientific) image analysis software.

### H. Inductively coupled plasma optical emission spectroscopy (ICP-OES)

The elemental composition of the NMC811 powder was determined using an Agilent 5110 inductively coupled plasma optical emission spectrometer. 50 mg of sample material was dissolved in a 5-ml mixture of ultratrace pure 37% HCl and 65% HNO<sub>3</sub> (3:1 v/v). In triplicate, the samples were heated to 115 °C for 45 min on a DigiPREP hot block (QMX Laboratories, UK). Prior to analysis, the sample solutions underwent a 1000× dilution with a 5% HNO<sub>3</sub> acid matrix.

### ACKNOWLEDGMENTS

This work was supported by the Faraday Institution Research Pouch Cell Manufacture (FIRG062) and Degradation (FIRG060) projects. The Faraday Institution Future-Cat (FIRG065) project is also acknowledged. Alexandra Morscher (University of Liverpool) is acknowledged for their input in the *operando* XRD data analysis. Dr. Matthew Capener (WMG, University of Warwick) is

also acknowledged for their inputs on pouch-cell fabrication. This project has been supported by the National Facility in X-Ray CT (EP/T02593X/1) and the International Centre to Centre partnership with the European Synchrotron Radiation Facility (ESRF) “Manufacturing by Design” (EP/W003333/1). Partha Paul (University of Manchester/ESRF) is acknowledged for support with the beamtime proposal. We also acknowledge the ESRF for provision of synchrotron radiation facilities and Dr. Dmitry Karpov, for assistance and support in using beam line ID16A.

- 
- [1] M. Jiang, D. L. Danilov, R.-A. Eichel, and P. H. L. Notten, A review of degradation mechanisms and recent achievements for Ni-rich cathode-based Li-ion batteries, *Adv. Energy Mater.* **11**, 2103005 (2021).
- [2] H. Zhang, H. Liu, L. F. J. Piper, M. S. Whittingham, and G. Zhou, Oxygen loss in layered oxide cathodes for Li-ion batteries: Mechanisms, effects, and mitigation, *Chem. Rev.* **122**, 5641 (2022).
- [3] H.-H. Ryu, K.-J. Park, C. S. Yoon, and Y.-K. Sun, Capacity fading of Ni-rich  $\text{Li}[\text{Ni}_x\text{Co}_y\text{Mn}_{1-x-y}]\text{O}_2$  ( $0.6 \leq x \leq 0.95$ ) cathodes for high-energy-density lithium-ion batteries: Bulk or surface degradation? *Chem. Mater.* **30**, 1155 (2018).
- [4] W. Li, H. Y. Asl, Q. Xie, and A. Manthiram, Collapse of  $\text{LiNi}_{1-x-y}\text{Co}_x\text{Mn}_y\text{O}_2$  lattice at deep charge irrespective of nickel content in lithium-ion batteries, *J. Am. Chem. Soc.* **141**, 5097 (2019).
- [5] H. Li, A. Liu, N. Zhang, Y. Wang, S. Yin, H. Wu, and J. R. Dahn, An unavoidable challenge for Ni-rich positive electrode materials for lithium-ion batteries, *Chem. Mater.* **31**, 7574 (2019).
- [6] K. Homlamai, N. Anansuksawat, N. Joraleechanchai, P. Chiochan, T. Sangsanit, W. Tejangkura, T. Maihom, J. Limtrakul, and M. Sawangphruk, Microcracking of Ni-rich layered oxide does not occur at single crystal primary particles even abused at 4.7 V, *Chem. Commun.* **58**, 11382 (2022).
- [7] J. Li, A. R. Cameron, H. Li, S. Glazier, D. Xiong, M. Chatzidakis, J. Allen, G. A. Botton, and J. R. Dahn, Comparison of single crystal and polycrystalline  $\text{LiNi}_{0.5}\text{Mn}_{0.3}\text{Co}_{0.2}\text{O}_2$  positive electrode materials for high voltage Li-ion cells, *J. Electrochem. Soc.* **164**, A1534 (2017).
- [8] T. M. M. Heenan, A. Wade, C. Tan, J. E. Parker, D. Matras, A. S. Leach, J. B. Robinson, A. Llewellyn, A. Dimitrijevic, R. Jervis, P. D. Quinn, D. J. L. Brett, and P. R. Shearing, Identifying the origins of microstructural defects such as cracking within Ni-rich NMC811 cathode particles for lithium-ion batteries, *Adv. Energy Mater.* **10**, 2002655 (2020).
- [9] Y. Bi, J. Tao, Y. Wu, L. Li, Y. Xu, E. Hu, B. Wu, J. Hu, C. Wang, J.-G. Zhang, Y. Qi, and J. Xiao, Reversible planar gliding and microcracking in a single-crystalline Ni-rich cathode, *Science* **370**, 1313 (2020).
- [10] H. Cha, J. Kim, H. Lee, N. Kim, J. Hwang, J. Sung, M. Yoon, K. Kim, and J. Cho, Boosting reaction homogeneity in high-energy lithium-ion battery cathode materials, *Adv. Mater.* **32**, 2003040 (2020).
- [11] H. Kaneda, Y. Furuichi, A. Ikezawa, and H. Arai, Single-crystal-like durable  $\text{LiNiO}_2$  positive electrode materials for lithium-ion batteries, *ACS Appl. Mater. Interfaces* **14**, 52766 (2022).
- [12] Y. Liu, J. Harlow, and J. Dahn, Microstructural observations of “single crystal” positive electrode materials before and after long term cycling by cross-section scanning electron microscopy, *J. Electrochem. Soc.* **167**, 020512 (2020).
- [13] S. Oswald, M. Bock, and H. A. Gasteiger, The implications of particle morphology on the capacity retention, side reactions, and impedance build-up of nickel-rich NCMs upon cycling in full-cells: Poly- vs. single-crystalline NCM851005, *J. Electrochem. Soc.* **170**, 090505 (2023).
- [14] W. Zhao, K. Wang, X. Fan, F. Ren, X. Xu, Y. Liu, S. Xiong, X. Liu, Z. Zhang, M. Si, R. Zhang, W. van den Bergh, P. Yan, C. Battaglia, T. Brezesinski, and Y. Yang, Quantifying degradation parameters of single-crystalline Ni-rich cathodes in lithium-ion batteries, *Angew. Chem., Int. Ed.* **62**, e202305281 (2023).
- [15] H.-H. Ryu, B. Namkoong, J.-H. Kim, I. Belharouak, C. S. Yoon, and Y.-K. Sun, Capacity fading mechanisms in Ni-rich single-crystal NCM cathodes, *ACS Energy Lett.* **6**, 2726 (2021).
- [16] P. Venkatachalam, C. Karra, K. K. Duru, P. S. Maram, S. Sambasivam, H. K. Liu, and S. Kalluri, Critical perspective on the industry-centred engineering of single-crystalline Ni-rich cathodes, *ChemNanoMat.* **9**, e202200548 (2023).
- [17] J. Xiao, F. Shi, T. Glossmann, C. Burnett, and Z. Liu, From laboratory innovations to materials manufacturing for lithium-based batteries, *Nat. Energy* **8**, 329 (2023).
- [18] K. Kleiner, D. Dixon, P. Jakes, J. Melke, M. Yavuz, C. Roth, K. Nikolowski, V. Liebau, and H. Ehrenberg, Fatigue of  $\text{LiNi}_{0.8}\text{Co}_{0.15}\text{Al}_{0.05}\text{O}_2$  in commercial Li ion batteries, *J. Power Sources* **273**, 70 (2015).
- [19] S. Schweidler, L. de Biasi, G. Garcia, A. Mazilkin, P. Hartmann, T. Brezesinski, and J. Janek, Investigation into mechanical degradation and fatigue of high-Ni NCM cathode material: A long-term cycling study of full cells, *ACS Appl. Energy Mater.* **2**, 7375 (2019).
- [20] C. Xu, K. Märker, J. Lee, A. Mahadevegowda, P. J. Reeves, S. J. Day, M. F. Groh, S. P. Emge, C. Ducati, B. Layla Mehdi, C. C. Tang, and C. P. Grey, Bulk fatigue induced by surface reconstruction in layered Ni-rich cathodes for Li-ion batteries, *Nat. Mater.* **20**, 84 (2021).
- [21] F. Friedrich, B. Strehle, A. T. S. Freiberg, K. Kleiner, S. J. Day, C. Erk, M. Piana, and H. A. Gasteiger, Editors’ choice—Capacity fading mechanisms of NCM-811 cathodes in lithium-ion batteries studied by x-ray diffraction and other diagnostics, *J. Electrochem. Soc.* **166**, A3760 (2019).
- [22] C. D. Quilty, P. J. West, G. P. Wheeler, L. M. Housel, C. J. Kern, K. R. Tallman, L. Ma, S. Ehrlich, C. Jaye, D. A. Fischer, K. J. Takeuchi, D. C. Bock, A. C. Marschilok, and E. S. Takeuchi, Elucidating cathode degradation mechanisms in  $\text{LiNi}_{0.8}\text{Mn}_{0.1}\text{Co}_{0.1}\text{O}_2$  (NMC811)/graphite cells under fast charge rates using *operando* synchrotron characterization, *J. Electrochem. Soc.* **169**, 020545 (2022).
- [23] H. Liu, M. Wolfman, K. Karki, Y.-S. Yu, E. A. Stach, J. Cabana, K. W. Chapman, and P. J. Chupas, Intergranular



- cracking as a major cause of long-term capacity fading of layered cathodes, *Nano Lett.* **17**, 3452 (2017).
- [24] W. M. Dose, J. K. Morzy, A. Mahadevegowda, C. Ducati, C. P. Grey, and M. F. L. De Volder, The influence of electrochemical cycling protocols on capacity loss in nickel-rich lithium-ion batteries, *J. Mater. Chem. A* **9**, 23582 (2021).
- [25] W. Li, X. Liu, Q. Xie, Y. You, M. Chi, and A. Manthiram, Long-term cyclability of NCM-811 at high voltages in lithium-ion batteries: An in-depth diagnostic study, *Chem. Mater.* **32**, 7796 (2020).
- [26] R. Jung, F. Linsenmann, R. Thomas, J. Wandt, S. Solchenbach, F. Maglia, C. Stinner, M. Tromp, and H. A. Gasteiger, Nickel, manganese, and cobalt dissolution from Ni-rich NMC and their effects on NMC622-graphite cells, *J. Electrochem. Soc.* **166**, A378 (2019).
- [27] J. A. Gilbert, I. A. Shkrob, D. P. Abraham, Transition metal dissolution, ion migration, electrocatalytic reduction and capacity loss in lithium-ion full cells, *J. Electrochem. Soc.* **164**, A389 (2017).
- [28] J. A. Gilbert, J. Bareño, T. Spila, S. E. Trask, D. J. Miller, B. J. Polzin, A. N. Jansen, and D. P. Abraham, Cycling behavior of NCM523/graphite lithium-ion cells in the 3–4.4 V range: Diagnostic studies of full cells and harvested electrodes, *J. Electrochem. Soc.* **164**, A6054 (2017).
- [29] J. S. Edge, *et al.*, Lithium ion battery degradation: What you need to know, *Phys. Chem. Chem. Phys.* **23**, 8200 (2021).
- [30] I. Bloom, J. Christophersen, and K. Gering, Differential voltage analyses of high-power lithium-ion cells: 2. Applications, *J. Power Sources* **139**, 304 (2005).
- [31] W. M. Dose, C. Xu, C. P. Grey, and M. F. L. De Volder, Effect of anode slippage on cathode cutoff potential and degradation mechanisms in Ni-rich Li-ion batteries, *Cell Rep. Phys. Sci.* **1**, 100253 (2020).
- [32] R. Jung, M. Metzger, F. Maglia, C. Stinner, and H. A. Gasteiger, Oxygen release and its effect on the cycling stability of  $\text{LiNi}_x\text{Mn}_y\text{Co}_z\text{O}_2$  (NMC) cathode materials for Li-ion batteries, *J. Electrochem. Soc.* **164**, A1361 (2017).
- [33] W. M. Dose, W. Li, I. Temprano, C. A. O’Keefe, B. L. Mehdi, M. F. L. De Volder, and C. P. Grey, Onset potential for electrolyte oxidation and Ni-rich cathode degradation in lithium-ion batteries, *ACS Energy Lett.* **7**, 3524 (2022).
- [34] G. J. Páez Fajardo, E. Fiamegkou, J. A. Gott, H. Wang, I. Temprano, I. D. Seymour, M. J. W. Ogley, A. S. Menon, I. E. L. Stephens, M. Ans, T.-L. Lee, P. K. Thakur, W. M. Dose, M. F. L. De Volder, C. P. Grey, and L. F. J. Piper, Synergistic degradation mechanism in single crystal Ni-rich NMC/graphite cells, *ACS Energy Lett.* **8**, 5025 (2023).
- [35] M. Wolfman, Y.-S. Yu, B. M. May, Z. W. Lebens-Higgins, S. Sallis, N. V. Faenza, N. Pereira, N. Shirato, V. Rose, D. A. Shapiro, G. G. Amatucci, L. F. J. Piper, and J. Cabana, Mapping competitive reduction upon charging in  $\text{LiNi}_{0.8}\text{Co}_{0.15}\text{Al}_{0.05}\text{O}_2$  primary particles, *Chem. Mater.* **32**, 6161 (2020).
- [36] J. Li, H. Liu, J. Xia, A. R. Cameron, M. Nie, G. A. Botton, and J. R. Dahn, The impact of electrolyte additives and upper cut-off voltage on the formation of a rocksalt surface layer in  $\text{LiNi}_{0.8}\text{Mn}_{0.1}\text{Co}_{0.1}\text{O}_2$  electrodes, *J. Electrochem. Soc.* **164**, A655 (2017).
- [37] Z. Ruff, C. Xu, and C. P. Grey, Transition metal dissolution and degradation in NMC811-graphite electrochemical cells, *J. Electrochem. Soc.* **168**, 060518 (2021).
- [38] O. C. Harris, S. E. Lee, C. Lees, and M. Tang, Review: Mechanisms and consequences of chemical cross-talk in advanced Li-ion batteries, *J. Phys.: Energy* **2**, 032002 (2020).
- [39] J. C. Hestenes and L. E. Marbella, Beyond composition: Surface reactivity and structural arrangement of the cathode-electrolyte interphase, *ACS Energy Lett.* **8**, 4572 (2023).
- [40] J. T. Frith, M. J. Lacey, and U. Ulissi, A non-academic perspective on the future of lithium-based batteries, *Nat. Commun.* **14**, 420 (2023).
- [41] A. Smith, P. Stüble, L. Leuthner, A. Hofmann, F. Jeschull, and L. Mereacre, Potential and limitations of research battery cell types for electrochemical data acquisition, *Batteries Supercaps* **6**, e202300080 (2023).
- [42] Z. Lin, T. Liu, X. Ai, and C. Liang, Aligning academia and industry for unified battery performance metrics, *Nat. Commun.* **9**, 5262 (2018).
- [43] D. Saurel, A. Pendashteh, M. Jáuregui, M. Reynaud, M. Fehse, M. Galceran, and M. Casas-Cabanas, Experimental considerations for *operando* metal-ion battery monitoring using x-ray techniques, *Chem.: Methods* **1**, 249 (2021).
- [44] S.-M. Bak, Z. Shadike, R. Lin, X. Yu, and X.-Q. Yang, In situ/operando synchrotron-based x-ray techniques for lithium-ion battery research, *NPG Asia Mater.* **10**, 563 (2018).
- [45] T. Taskovic, A. Eldesoky, W. Song, M. Bauer, and J. R. Dahn, High temperature testing of NMC/graphite cells for rapid cell performance screening and studies of electrolyte degradation, *J. Electrochem. Soc.* **169**, 040538 (2022).
- [46] A. Eldesoky, M. Bauer, S. Azam, E. Zsoldos, W. Song, R. Weber, S. Hy, M. B. Johnson, M. Metzger, and J. R. Dahn, Impact of graphite materials on the lifetime of NMC811/graphite pouch cells: part I. Material properties, arc safety tests, gas generation, and room temperature cycling, *J. Electrochem. Soc.* **168**, 110543 (2021).
- [47] H. Michael, R. E. Owen, J. B. Robinson, T. M. M. Heenan, C. Tan, A. J. Wade, R. Jervis, D. J. L. Brett, and P. R. Shearing, Correlative electrochemical acoustic time-of-flight spectroscopy and x-ray imaging to monitor the performance of single-crystal and polycrystalline NMC811/Gr lithium-ion batteries, *J. Power Sources* **542**, 231775 (2022).
- [48] R. Weber, C. R. Fell, J. R. Dahn, and S. Hy, Operando x-ray diffraction study of polycrystalline and single-crystal  $\text{Li}_x\text{Ni}_{0.5}\text{Mn}_{0.3}\text{Co}_{0.2}\text{O}_2$ , *J. Electrochem. Soc.* **164**, A2992 (2017).
- [49] G. J. Páez Fajardo, M. Belekoukia, S. Bolloju, E. Fiamegkou, A. S. Menon, Z. Ruff, Z. Shen, N. Shah, E. Björklund, M. J. Zuba, T.-L. Lee, P. K. Thakur, R. S. Weatherup, A. Aguadero, M. J. Loveridge, C. P. Grey, and L. F. J. Piper, Understanding improved capacity retention at 4.3 V in modified single crystal Ni-rich NMC/graphite pouch cells at elevated temperature, *RSC Appl. Interfaces* **1**, 133 (2024).
- [50] R. S. Arumugam, L. Ma, J. Li, X. Xia, J. M. Paulsen, and J. R. Dahn, Special synergy between electrolyte additives and positive electrode surface coating to enhance



- the performance of  $\text{Li}[\text{Ni}_{0.6}\text{Mn}_{0.2}\text{Co}_{0.2}]\text{O}_2/\text{graphite}$  cells, *J. Electrochem. Soc.* **163**, A2531 (2016).
- [51] R. S. Negi, S. P. Culver, A. Mazilkin, T. Brezesinski, and M. T. Elm, Enhancing the electrochemical performance of  $\text{LiNi}_{0.70}\text{Co}_{0.15}\text{Mn}_{0.15}\text{O}_2$  cathodes using a practical solution-based  $\text{Al}_2\text{O}_3$  coating, *ACS Appl. Mater. Interfaces* **12**, 31392 (2020).
- [52] D. S. Hall, R. Gauthier, A. Eldesoky, V. S. Murray, and J. R. Dahn, New chemical insights into the beneficial role of  $\text{Al}_2\text{O}_3$  cathode coatings in lithium-ion cells, *ACS Appl. Mater. Interfaces* **11**, 14095 (2019).
- [53] I. Buchberger, S. Seidlmayer, A. Pokharel, M. Piana, J. Hattendorff, P. Kudejova, R. Gilles, and H. A. Gasteiger, Aging analysis of graphite/ $\text{LiNi}_{1/3}\text{Mn}_{1/3}\text{Co}_{1/3}\text{O}_2$  cells using XRD, PGAA, and ac impedance, *J. Electrochem. Soc.* **162**, A2737 (2015).
- [54] J. E. Harlow, S. L. Glazier, J. Li, and J. R. Dahn, Use of asymmetric average charge- and average discharge- voltages as an indicator of the onset of unwanted lithium deposition in lithium-ion cells, *J. Electrochem. Soc.* **165**, A3595 (2018).
- [55] T. Momma, T. Yokoshima, H. Nara, Y. Gima, and T. Osaka, Distinction of impedance responses of Li-ion batteries for individual electrodes using symmetric cells, *Electrochim. Acta* **131**, 195 (2014).
- [56] T. F. Landler, G. Schwarzberger, and A. Jossen, High frequency impedance characteristics of cylindrical lithium-ion cells: Physical-based modeling of cell state and cell design dependencies, *J. Power Sources* **488**, 229463 (2021).
- [57] A. S. Leach, A. V. Llewellyn, C. Xu, C. Tan, T. M. M. Heenan, A. Dimitrijevic, K. Kleiner, C. P. Grey, D. J. L. Brett, C. C. Tang, P. R. Shearing, and R. Jervis, Spatially resolved operando synchrotron-based x-ray diffraction measurements of Ni-rich cathodes for Li-ion batteries, *Front. Chem. Eng.* **3**, 794194 (2022).
- [58] K. Kleiner, C. A. Murray, C. Grosu, B. Ying, M. Winter, P. Nagel, S. Schuppler, and M. Merz, On the origin of reversible and irreversible reactions in  $\text{LiNi}_x\text{Co}_{(1-x)/2}\text{Mn}_{(1-x)/2}\text{O}_2$ , *J. Electrochem. Soc.* **168**, 120533 (2021).
- [59] W. E. O'Grady, K. I. Pandya, K. E. Swider, and D. A. Corrigan, *In situ* x-ray absorption near-edge structure evidence for quadrivalent nickel in nickel battery electrodes, *J. Electrochem. Soc.* **143**, 1613 (1996).
- [60] A. S. Menon, B. J. Johnston, S. G. Booth, L. Zhang, K. Kress, B. E. Murdock, G. Paez Fajardo, N. N. Anthonisamy, N. Tapia-Ruiz, S. Agrestini, M. Garcia-Fernandez, K. Zhou, P. K. Thakur, T. L. Lee, A. J. Nedoma, S. A. Cussen, and L. F. J. Piper, Oxygen-redox activity in non-lithium-excess tungsten-doped  $\text{LiNiO}_2$  cathode, *PRX Energy* **2**, 013005 (2023).
- [61] A. R. Genreith-Schriever, H. Banerjee, A. S. Menon, E. N. Bassey, L. F. J. Piper, C. P. Grey, and A. J. Morris, Oxygen hole formation controls stability in  $\text{LiNiO}_2$  cathodes, *Joule* **7**, 1623 (2023).
- [62] S. S. Pandurangi, D. S. Hall, C. P. Grey, V. S. Deshpande, and N. A. Fleck, Chemo-mechanical analysis of lithiation/delithiation of Ni-rich single crystals, *J. Electrochem. Soc.* **170**, 050531 (2023).
- [63] H. M. Rietveld, Line profiles of neutron powder-diffraction peaks for structure refinement, *Acta Crystallogr.* **22**, 151 (1967).
- [64] H. M. Rietveld, A profile refinement method for nuclear and magnetic structures, *J. Appl. Crystallogr.* **2**, 65 (1969).
- [65] G. S. Pawley, Unit-cell refinement from powder diffraction scans, *J. Appl. Crystallogr.* **14**, 357 (1981).
- [66] A. A. Coelho, TOPAS and TOPAS-ACADEMIC: An optimization program integrating computer algebra and crystallographic objects written in C++, *J. Appl. Crystallogr.* **51**, 210 (2018).
- [67] E. P. Jahrman, W. M. Holden, A. S. Ditter, D. R. Mortensen, G. T. Seidler, T. T. Fister, S. A. Kozimor, L. F. J. Piper, J. Rana, N. C. Hyatt, and M. C. Stennett, An improved laboratory-based x-ray absorption fine structure and x-ray emission spectrometer for analytical applications in materials chemistry research, *Rev. Sci. Instrum.* **90**, 024106 (2019).
- [68] B. Ravel and M. Newville, ATHENA, ARTEMIS, HEPHAESTUS: Data analysis for x-ray absorption spectroscopy using IFFFIT, *J. Synchrotron Radiat.* **12**, 537 (2005).
- [69] K. K. Neelisetty, J. Stetina, J. Vondruška, M. Trenz, T. Kazda, M. Hrouzek, and P. Wandrol, Transfer of lithium foil under inert conditions using CleanConnect inert gas transfer system, *Microsc. Microanal.* **27**, 2508 (2021).
- [70] DRAGONFLY 2020.2 (computer software). Object Research Systems (Ors) Inc., Montreal, Canada, 2020; software available at <http://www.Theobjects.Com/Dragonfly>
- [71] C. d. S. Julio, H. Jan, R. Guillermo, H. Maxime, P. Alexandra, B. Leonid, Y. Yang, and C. Peter, in *High Energy Near- and Far-Field Ptychographic Tomography at the ESRF, Developments in X-Ray Tomography XI* (SPIE, 2017). Vol. 10391.
- [72] R. Mokso, P. Cloetens, E. Maire, W. Ludwig, and J. Y. Buffière, Nanoscale zoom tomography with hard x rays using Kirkpatrick-Baez optics, *Appl. Phys. Lett.* **90**, 144104 (2007).
- [73] See the Supplemental Material at <http://link.aps.org/supplemental/10.1103/PRXEnergy.3.013004> for further electrochemical and characterization data from the experiments, including high-resolution SEM and x-ray media files. Pertinent raw data files from the experiments are also included.